scientific reports

OPEN

Scalable synthesis of millimeter-long single crystal Ta$_2$Ni$_3$Se$_8$ Van der Waals nanowires

Abin Joshy[1], Fei Wang[1], Sidra Younus[1], Keyuan Bai[1], Konstantin V. Larionov[2], Liubov Yu. Antipina[2], Pavel B. Sorokin[2,4], Yun Ling[3] & Jiang Wei[1✉]

One-dimensional (1D) van der Waals (vdW) nanowires, formed from molecular chains bonded through weak interactions, represent a significant departure from traditional nanowires by offering the potential to miniaturize functional devices to the molecular scale while maintaining crystallinity, a feature attributable to their exfoliable nature and chemically inert surfaces. However, the lack of efficient synthesis methods has hindered the exploration of their intrinsic properties and potential applications. The production of vdW nanowires has predominantly relied on the exfoliation of bulk crystals, leaving their direct synthesis largely unexplored. In this work, we introduce a novel solid-state growth technique that facilitates the high-yield and scalable fabrication of single-crystal Ta$_2$Ni$_3$Se$_8$ (TNS) nanowires, achieving a consistent thickness of 100 nm and lengths extending to several millimeters. We further demonstrate a few centimeter scale alignments of as-grown nanowires and show that these nanowires can be easily dry exfoliated to produce several nanometer-thick, air-stable nanowires. Employing density functional theory, we investigate the bonding characteristics within these nanowires, identifying a highly anisotropic bonding density that significantly contributes to their facile exfoliation. Moreover, the development of Schottky device arrays on individual TNS nanowires and subsequent electrical transport measurements affirm the uniform Schottky contact properties along their entire length, characterized by a barrier height of approximately 0.39 eV. The successful synthesis of structurally and electronically uniform, ultralong TNS nanowires may open a new avenue in developing integrated molecular electronics and sensors using 1D vdW materials.

Keywords Van der Waals nanowires, 1D semiconductor, Nanowire alignment, Nano-electronic devices, Schottky barrier

Two dimensional (2D) van der Waals (vdW) materials uncovered novel electrical properties due to quantum confinement effect and reduced symmetry, allowing investigation of thickness dependent bandgaps[1], topological phase transition[2], excitons[3], and valley polarization[4,5], enabling their application in electronics and sensors. On the other hand, one-dimensional (1D) vdW materials, made of 1D molecular chains, extend dimensional confinement further. Within each chain, atoms are connected through covalent bonds, while in between chains, vdW-like weak bonding interaction holds chains together to form a single crystal. Such 1D vdW materials with strict 1D confinement, large surface-to-volume ratio, and strong electron-electron interaction bring new physics for fundamental research and technological applications. Examples include the highly anisotropic conductivity of TiS$_3$[6,7] and the significant breakdown current density found in TaSe$_3$[8] and ZrTe$_3$ nanoribbons[9] Ballistic heat transport has been discovered in Ta$_2$Pd$_3$Se$_8$[10] High anisotropy in optical absorption/emission has been demonstrated in ZrS$_3$[11] In addition, the applications of interconnects,[12] field-effect transistors (FET),[13] and photodetectors[14] have been demonstrated. However, unlike the blooming number of 2D vdW materials, a very limited number of 1D vdW materials have been studied briefly, which include transition metal trichalcogenides MX$_3$ (M = Ti, Nb, Ta, Zr; X = S, Se, Te)[15–18] ternary transition metal chalcogenides M$_2$X$_3$Y$_8$ (M = Ta, Nb; X = Ni, Pd, Pt; Y = S, Se),[19–22] Nb$_2$Se$_9$,[23] SnIP,[24] Mo$_6$S$_3$I$_6$,[25] CrSbSe$_3$,[26,27] Sb$_2$Se$_3$,[28] red phosphorous,[29] and tellurium[30].

The scarcity of methods for producing van der Waals (vdW) nanowires is a significant obstacle in advancing research in this domain. Currently, exfoliation is the primary technique for fabricating vdW nanowires,

[1]Physics and Engineering Physics, Tulane University, New Orleans, LA 70118, USA. [2]Laboratory of Digital Material Science, National University of Science and Technology MISiS, Moscow 119049, Russia. [3]College of Electronic and Information Engineering, Suzhou University of Science and Technology, Suzhou 215011, Jiangsu, China. [4]Institute of Microelectronics Technology and High-Purity Materials, Russian Academy of Sciences, Chernogolovka, Russian Federation. ✉email: jwei1@tulane.edu

involving the separation of bulk crystals through mechanical means such as tape[20] or ultrasonic treatment in liquids[31] While the tape method can produce high-quality nanowires, its drawbacks include low yield and shorter nanowire lengths. On the other hand, liquid exfoliation offers improved yields but tends to result in nanowire breakage and the introduction of defects[32,33] To date, there have been no comprehensive reports of direct methods for synthesizing vdW nanowires, which is likely due to the complexities involved in the chemical reactions and growth processes. Therefore, developing a straightforward approach for the mass production of single-crystal vdW nanowires with high aspect ratios, uniform structural integrity, and dependable electrical properties is highly desirable. Such an advancement would greatly enhance the integration of these nanowires into a variety of functional devices, broadening their application potential.

In this study, we present a method for synthesizing semiconducting $Ta_2Ni_3Se_8$ (TNS)[34] vdW nanowires through a single-step solid-state reaction. The approach used in this work is both straightforward and cost-effective, resulting in the production of large-scale, mm-long TNS nanowires with uniform morphology and aspect ratios exceeding 10,000. Following growth, mechanical exfoliation was demonstrated to produce nanowires with thicknesses down to a few nanometers. Transmission electron microscopy (TEM) revealed that the TNS nanowires are homogeneous single crystals that remain resistant to oxidation at room temperature. Additionally, TNS nanowire-based nanodevices were fabricated with nickel contacts, which exhibit Schottky diode properties with a barrier height of approximately 0.39 eV.

Results and discussion

The growth of TNS nanowires is achieved through a straightforward and reliable solid-state reaction, as illustrated in Fig. 1a (see methods for detail). Right after the growth, the product inside the sealed ampule (shown in Fig. 1b) seems to be composed of tightly packed nanowires resembling a turf of rolling grass. After gently cutting the ampule open, the turf roll was transferred out with its outer surface wrapped with Scotch tape. With this process, the original shape of the turf roll is preserved for further investigation. As shown in Fig. 1c, the as-grown nanowires extended from the inner wall of the ampule to the central region to form a single-piece turf roll. The growth mechanism will be discussed in detail in the following section. In order to conduct a comprehensive morphology analysis, the turf roll is then cut open along the longitudinal direction and unfolded on the substrate.

The TNS turf roll is first examined using a scanning electron microscope (SEM) by taking high-resolution micrographs of the nanowire at various locations. Figure 1d shows the unfolded turf roll lying flat on Scotch tape. The whole image is formed by stitching 64 SEM images, demonstrating the abundance of the growth. Figure 1e shows a side view of a flattened TNS turf, which exhibits an overall 2 mm thickness measured from the baseline. Most of the nanowires can be seen to extend from the bottom to the top, which suggests that each nanowire may be a few millimeters long on average. More SEM examinations of the nanowires on the bottom side surface of the turf (i.e., the outer surface of the turf roll) are shown in Figure S1a, b. We observe brighter regions or spots scattered throughout the bottom surface, which are clusters of significantly shorter nanowires. However, the top side of the turf (i.e., the central region of the turf roll), as shown in Figure S1c, d, is free of cluster regions and fully covered with clean and long nanowires. Therefore, we speculate that cluster regions may serve as seed sites during the growth, mostly located on the inner sidewall of the ampule. Nanowires grow from the cluster regions toward the center of the ampule, eventually form a turf structure.

We further suspect that the source particles, initially attached to the inner wall, form the seeding area that leads to abundant nanowire growth. To verify this hypothesis, we prepared two ampules, one with source powders covering only two ends of the ampule with an uncovered region in the center (Ampoule A) and the other with powder covering the entire inner wall (Ampoule B). This is realized by rubbing an O-ring on the outer surface of the ampule to induce electrostatic charges, which attract the source powder to the inner wall of the ampule. Then, the growth in both ampoules was conducted in the same conditions (see Figure S2a & d) simultaneously. The resulting ampules showed distinctive growth yield, as illustrated in Figures S2b & e. After opening the ampule, it was clear that the ampule with seeds covering the entire wall resulted in a dense growth of nanowires (Figure S2c & f). Complementary to the earlier understanding, this result provides strong evidence of the direct correlation between seeding source particles and nanowire growth.

It is worth emphasizing, in contrast to the synthesis approach[34] reported previously, which involves placing the elemental precursors (Ta, Ni, and Se powders) into a fixed location within the ampule, our method disperses the powder mixture uniformly across the entire inner surface of the quartz ampule. This is achieved through a simple yet effective electrostatic charging technique that promotes adhesion of the nano/micropowder onto the ampule walls. As a result, the growth initiates from spatially separated precursor particles, facilitating individual nucleation and sustained one-dimensional growth of nanowires. This dispersed growth environment prevents the aggregation seen in conventional bulk growth. Therefore, we recognize that this distributed nucleation mechanism, made possible by the electrostatic-assisted powder dispersion, is the central factor enabling the abundant formation of long and thin nanowires.

EDS and X-ray diffraction (XRD) characterizations were performed on the as-grown nanowires to assess their chemical composition and crystal structure. Figure S3a shows EDS data obtained from a collection of free-standing nanowires. All the peaks belong to the expected Ta, Ni, and Se, except C and O, due to carbon tape as the sample mount. A quantitative EDS analysis shows that the atomic ratio of Ta/Ni/Se is about 2:3:8, consistent with the stoichiometric ratio of the TNS crystal. Further, the seed region exhibited the same stoichiometric ratio, as shown in Figure S3b–d. The crystal structure of as-grown samples was determined by comparing our XRD powder diffraction peaks to those from the database (PDF#86-0186) (Figure S4a). All the XRD peaks matched with orthorhombic $Ta_2Ni_3Se_8$, as shown in Figure S4b–d, except for a few extra minor peaks, which correspond to monoclinic Ta_2NiSe_7. The two phases can be further estimated by comparing the weights of major peak
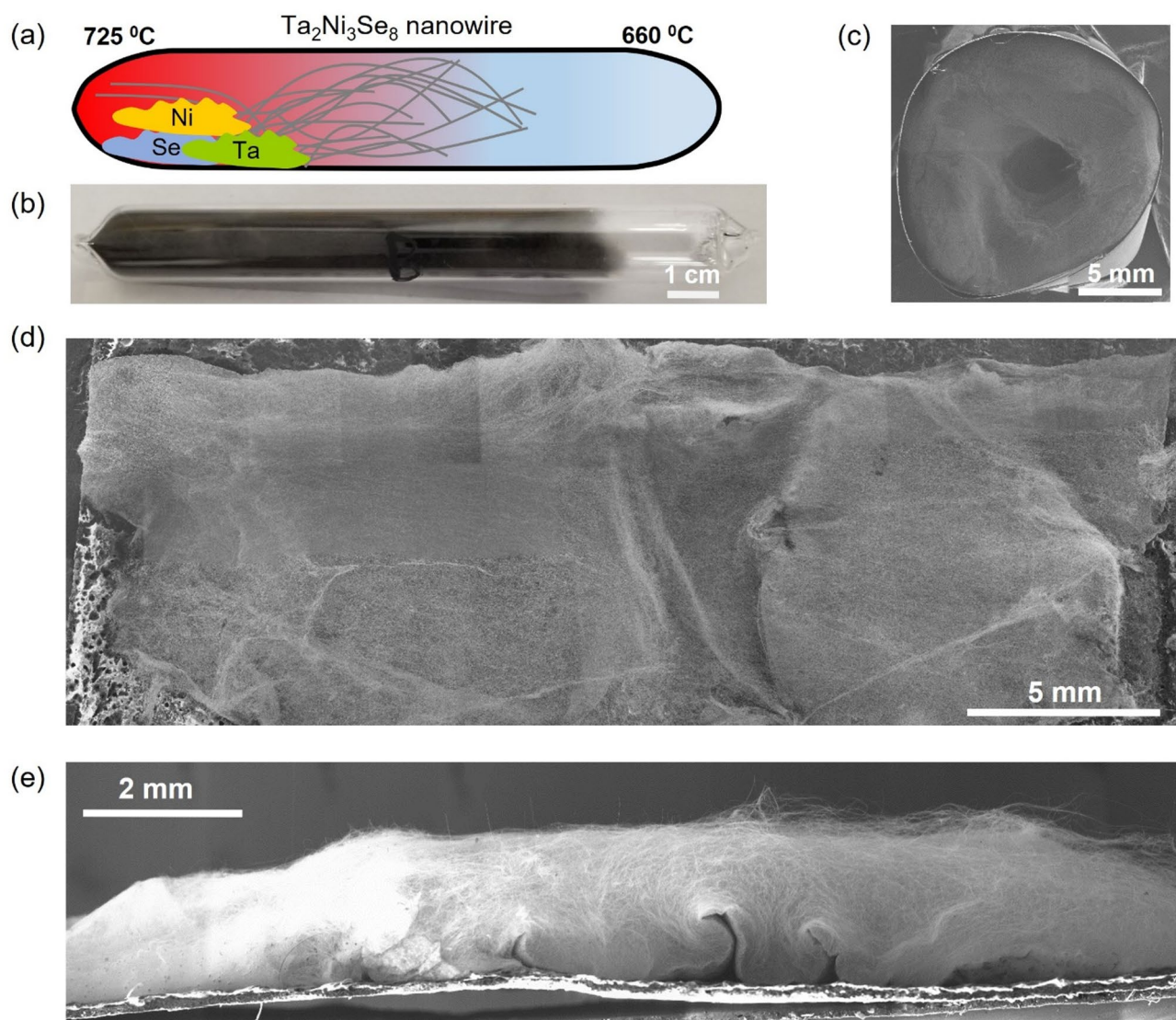
Fig. 1. Synthesis of crystalline TNS nanowires using solid-state growth. (**a**) Schematic of TNS nanowire growth via the solid-state reaction. (**b**) Photograph of the ampoule containing TNS nanowires after synthesis. (**c**) SEM image of the TNS turf roll after removing from the ampule, showing a cross-section relative to the ampule's longitudinal direction (Scotch tape is attached to the perimeter to maintain the shape of the turf roll). (**d**) SEM image of the unfolded TNS turf roll (obtained by stitching 64 SEM images) showing the overall size of grown TNS nanowire turf. (**e**) Side view of the turf roll section shown in (**d**).

profiles (see supplementary Figure S4e for more details). The as-grown nanowires contain 84.3 wt% $Ta_2Ni_3Se_8$ crystals and 15.7 wt% Ta_2NiSe_7 crystals.

The as-grown TNS nanowires are long but entangled, making it difficult to align or isolate them for further characterization. Therefore, we adopted a soft-lock drawing method[35] to align the nanowires from the turf roll. First, we cut and lay flat a piece of as-grown turf roll onto a silicon wafer. With a razor blade press hold still onto one side of the roll, another razor blade, wrapped with an ethanol-wetted nylon filter membrane, was press swept away from the fixed side, leaving behind a region with well-aligned nanowires, as shown in Fig. 2a. The ethanol acts as a lubricant to reduce the friction between the nanowire and the substrate. The razor blades were kept static for a few seconds after finishing the sweeping to prevent nanowires from retracting until the solvent evaporated.

After the alignment process, nanowires become untangled and straightened, ready to be picked up with tweezers and transferred onto other substrates for SEM examination. As shown in Fig. 2b, a typical single nanowire with a length reaching 2.1 mm can be easily placed onto carbon tape. The thickness is measured by taking high magnification images, as shown in Fig. 2c–g. By surveying multiple locations across the whole length, a highly uniform thickness of 260 nm with 5 nm variation is confirmed. In addition, we sampled about 200 nanowires, with the longest nanowire reaching 4 mm. The statistical analysis of the nanowire thickness
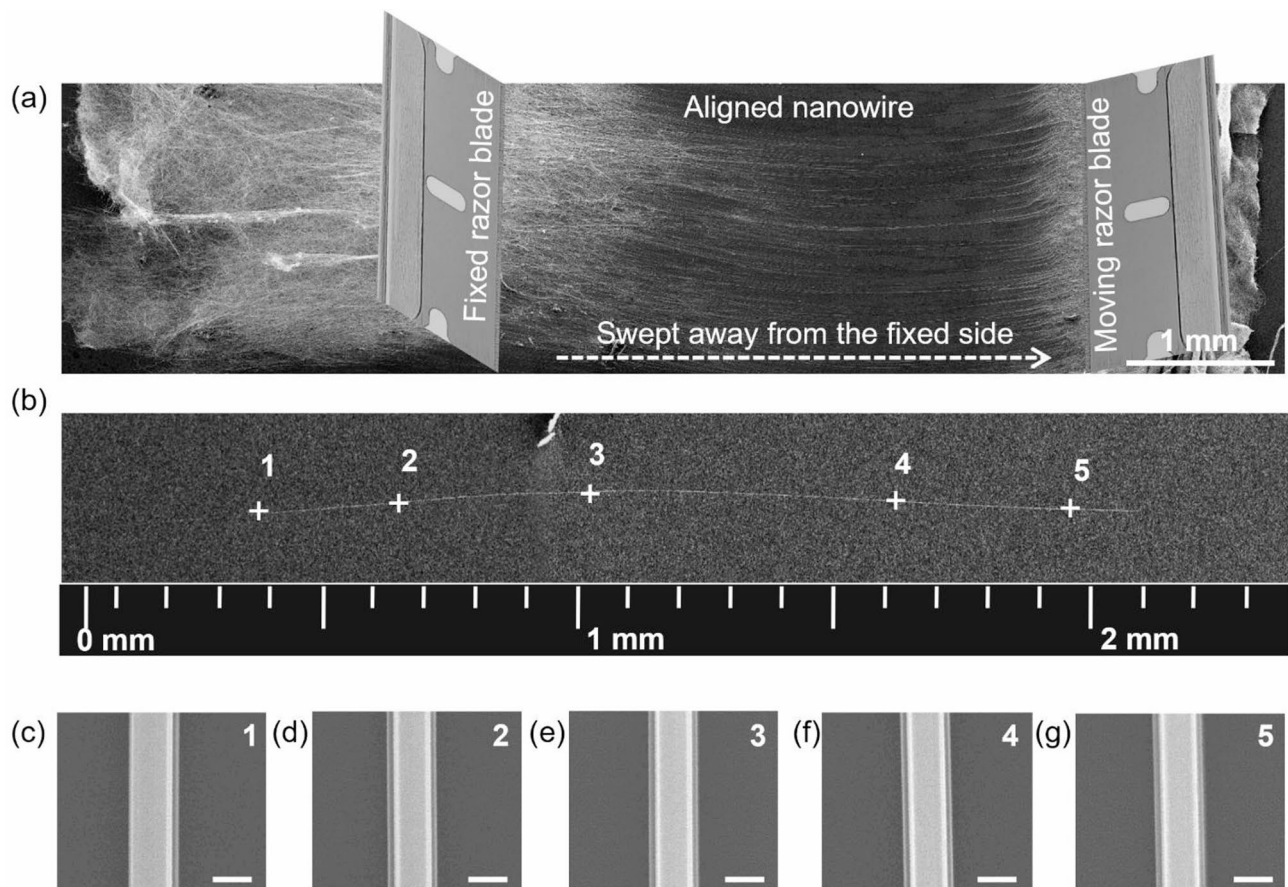
Fig. 2. Alignment of millimeter-long TNS nanowires. (**a**) Low-magnification SEM image of TNS nanowires aligned using the soft-lock drawing method. (**b**) SEM image of an isolated nanowire obtained through alignment. (**c**)–(**g**) High magnification SEM images of nanowire segment marked by white crosses in (**b**). The scale bar in (**c**)–(**g**) is 200 nm.

(shown in Figure S5) reveals that thicknesses distribute mostly between 100 and 400 nm with a frequently observed value of 170 nm.

Ultralong TNS nanowires have been successfully mass-produced through a straightforward solid-state reaction. To examine the crystallinity, structure integrity, and uniformity of the as-grown nanowires, TEM studies have been carried out. We prepared the TEM samples by gently rubbing the nanowire bundles directly onto TEM grids. A typical TNS nanowire obtained with this method shows a thickness of 30 nm, directly measured from the high-resolution TEM image, as illustrated in Fig. 3a. The high-resolution TEM image exhibits well-resolved lattice fringes of the nanowire (highlighted in the lower left inset) resulting from the projection of the (2 1 0) lattice planes, which is determined from the selective area electron diffraction (SAED) (top right inset). A direct measurement of the spacing between (2 1 0) planes is about 0.62 nm, consistent with the XRD data (as mentioned in Figure S4). The lower left inset highlights that the atomic-level clarity of molecular chains is most pronounced on the edge of the nanowire. Additionally, neither the edge nor the surface revealed any amorphous layer associated with lattice degradation or defects, which suggests the environmental stability of the structure. This result is also supported by theoretical prediction[36].

By comparing diffraction patterns taken from different incident angles of the electron beam, we found that the nanowire was grown along the [001] direction. In order to check the crystallinity of the nanowire, SAED was conducted on a 23 μm-long nanowire (shown in Fig. 3b). All five different locations along the nanowire were randomly selected for detailed investigation, as shown in Fig. 3c. They exhibit an identical diffraction pattern but with varying intensities, indicating a slight twist occurred when the nanowire was placed on the TEM grid, as shown in the insets of SAED pattern. Notably, a thorough investigation has been conducted on many nanowires, yielding consistent outcomes that suggest the predominance of single crystal structures in the TNS nanowires. In addition, we have assessed the ambient stability of the TNS nanowires and found them to exhibit strong resistance to degradation over time. Intermittent TEM measurements over one month were conducted, and no signs of amorphization or structural deterioration were observed. TEM images shown in Fig. 3 also represent our typical observation of the wire after long-term storage in an ambient environment. This observation is consistent with our previous DFT study on the isostructural compound $Ta_2Pd_3Se_8$ (Ref.[21]), where we calculated the adsorption energies of O_2 and H_2O molecules on the nanowire surface. The results
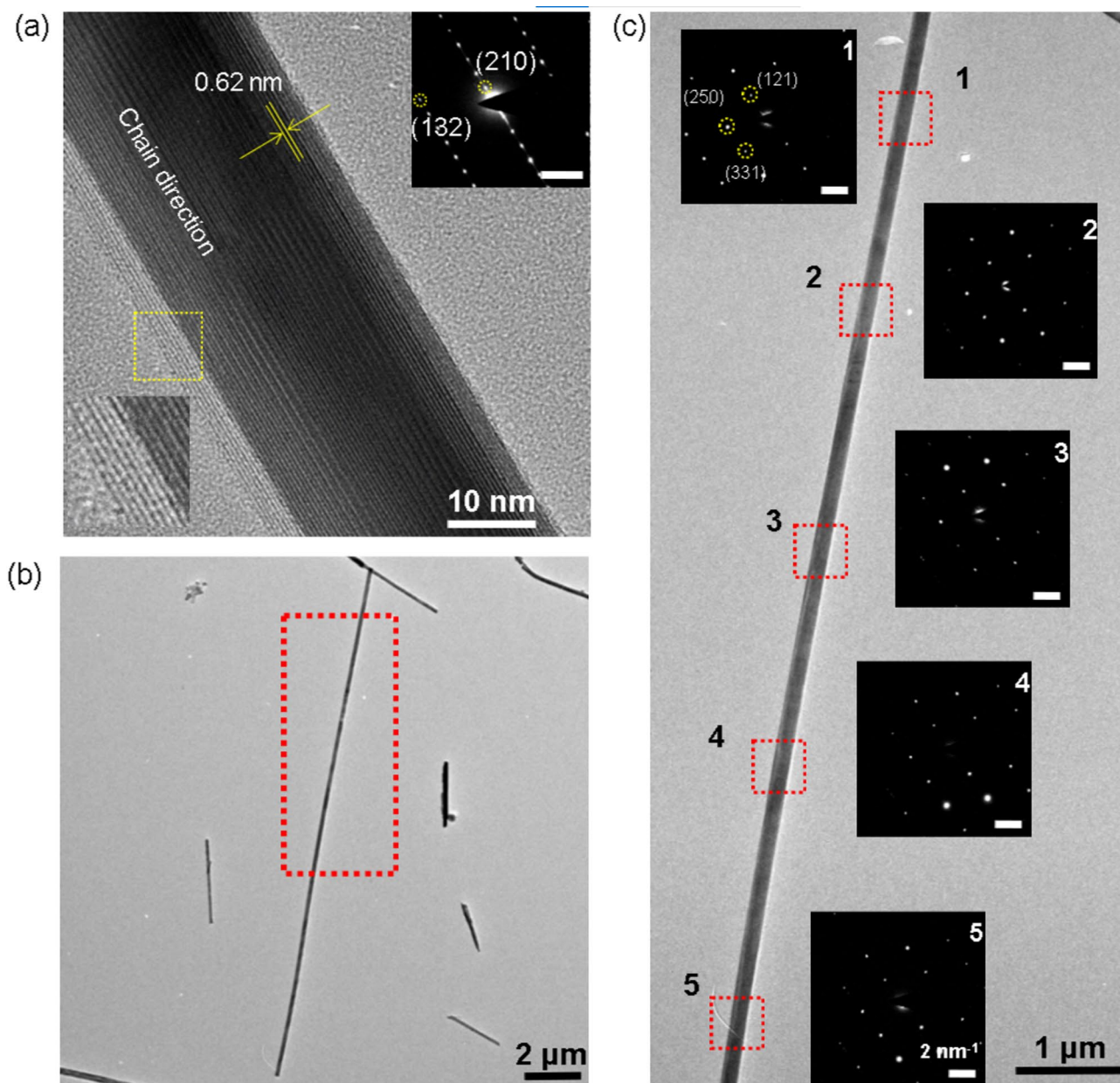
Fig. 3. Transmission-electron-microscopy analysis of ultralong $Ta_2Ni_3Se_8$ nanowires. (**a**) High-resolution TEM image of a representative nanowire. Lattice fringes with an interplanar spacing of 0.62 nm are clearly resolved perpendicular to the chain-growth direction. Inset: selected-area electron-diffraction (SAED) pattern indexed to monoclinic $Ta_2Ni_3Se_8$ (scale bar = 2 nm^{-1}). (**b**) The low-magnification survey TEM image displays a sparse network of nanowires. The nanowire outlined by the red dashed box was chosen for detailed crystallographic examination (scale bar = 2 μm). (**c**) Bright-field TEM image of the selected nanowire. SAED patterns were recorded at five positions (boxes 1–5) along its length; the identical spot patterns (insets, scale bars = 2 nm^{-1} demonstrate single-crystallinity and a uniform crystal orientation throughout the entire wire.

showed positive adsorption energies, indicating that stable adsorption of these ambient species is energetically unfavorable. This suggests that surface-driven degradation under ambient conditions is unlikely.

Based on the XRD and TEM analysis, it can be concluded that TNS belongs to the isostructural category of $M_2X_3Se_8$ (M = Ta or Nb; X = Ni, Pd, or Pt), with the orthorhombic space group D_{2h}^9- *Pbam*[37] As depicted in Fig. 4a–b, its crystal structure resembles a framework of molecular ribbons extending along the c-axis. Each ribbon (Fig. 4c) consists of two edge-sharing Ta-centered trigonal Se prism chains. They are connected at the ribbon's center and capped on both sides with Ni atoms. In order to form a bulk, TNS molecular ribbons are joined by interactions between the edge-terminating Ni atoms and the trans-Se atoms. Such interaction also slightly distorts the Se prisms. Overall, the bulk crystal can be viewed as composed of "windmill" units. Each unit includes four molecular ribbons rotated 90 degrees with a sizable channel in the center.
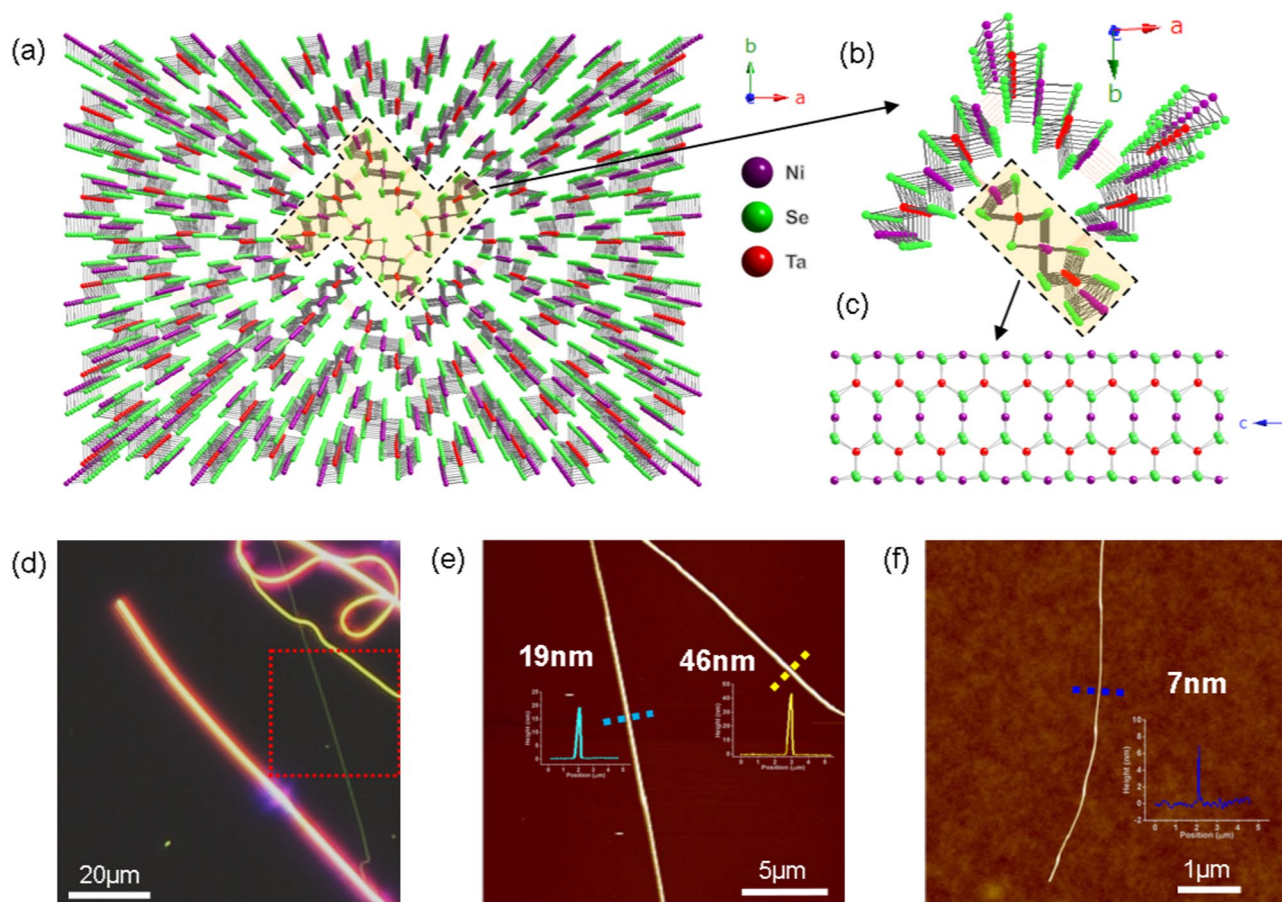
Fig. 4. Crystal structure and exfoliation of nanowires. (**a**) Stereo-view of TNS bulk crystal structure projected along the c-axis. (**b**) The 4-blade "windmill" unit is highlighted from the bulk TNS structure. (**c**) Top view of a single ribbon extended along the c direction. (**d**) Optical image of exfoliated TNS nanowires under darkfield illumination (**e**) AFM image of the region marked by a dashed rectangle in (**d**) showing nanowires with 19 nm and 46 nm thickness. (**f**) AFM image of a thin nanowire with a thickness of approximately 7 nm.

Due to the pronounced anisotropy of TNS crystal structure, it is hypothesized that a notable disparity in strength might exist between inter-molecular-chain and intra-molecular-chain bonds. Consequently, it is reasonable to anticipate that the TNS crystal may exhibit a propensity for facile cleavage along the directions of the molecular chains. Indeed, we demonstrate that thinner TNS nanowires can be further obtained from as-grown nanowires using mechanical exfoliation, which has been widely used in 2D materials[38] The as-grown TNS nanowire was first transferred onto Scotch tape, and the tape was then folded and split repeatedly, resulting in areas on the tape covered with a high density of thinned nanowires. Subsequently, the tape was applied onto a silicon wafer and peeled off, leading to the deposition of nanowires onto the substrate. The exfoliated nanowire was initially examined using an optical microscope. It is worth mentioning that dark field illumination significantly improved the detectability of nanowires with smaller diameters. As depicted in Fig. 4d, nanowires as thin as 19 nm are still visible under the dark field. It is evident that the TNS nanowires exhibit distinct color variations that correlate to varying thicknesses. This phenomenon might potentially be attributed to the scattering of light, which is limited by the size of the nanowires. However, further examination is required to gain a comprehensive understanding of this phenomenon. The accurate thicknesses of exfoliated nanowires, first observed in the optical microscope, can be further identified by atomic force microscopy (AFM), as shown in Fig. 4e. A thorough analysis using AFM was conducted on the exfoliated nanowires, leading to the conclusion that achieving TNS nanowires with a thickness as low as 7 nm is feasible (see Fig. 4f).

With the exfoliation of TNS nanowires demonstrated, the detailed mechanism still needs to be clarified. Conventional exfoliable materials, such as graphene, have been mostly known for processing a crystal structure with existing van der Waals bonds that are significantly weaker than chemical bonds. Such high anisotropy of bonding strengths enables mechanical exfoliation. Here, in TNS, exfoliation happens between the molecular chains. The inter-chain bonds, however, initially formed between nickel and selenium atoms, seem[39,40] and later confirmed (see analysis in supplementary Figures S6 & 7) as typical chemical bonds. Despite the absence of vdW bonds, TNS nevertheless has exceptional exfoliation properties. To elucidate this intricate scenario, a new perspective is required. Consequently, we performed a thorough computational density functional theory (DFT) analysis to model the exfoliation mechanism. Four possible cleavage bonds (labeled E_1 to E_4) exist in a

TNS crystal, as shown in Figure S7a. All bonds (E_1–E_4) possess comparable binding energy varying from 1.5 to 1.9 eV, which falls in the range of conventional chemical bonds[41] However, the possibility of a crystal being exfoliated along each specified surface should only be inversely proportional to the cleavage energy density, defined as the product of binding energy and bond density (i.e., bonds per unit surface area). Viewing from the TNS crystal structure, it is obvious that the bonding density on the surface intercepting with the chain is much higher than that along the chain. Further, on surfaces parallel to the chain, the inter or intra-chain bond density can vary significantly (see Figure S7b). The net cleavage energy from the surface only containing E_1 bonds (i.e., the inter-chain bond) is the lowest (6.24 eV) in comparison with that from other surfaces containing E_2 (15.52 eV), E_3 (26.72 eV), or E_4 (12.32 eV) bonds (i.e., the intra-chain bonds). Therefore, if the external force is applied, we expect the nanowire incline to split along the surface, where E_1 crosses through and breaks. This calculation agrees with the result of the exfoliation revealed from the TEM observation. Thus, it is important to note that bond density plays a vital role in enabling mechanical exfoliation in vdW-bonds-free crystals. The new exfoliation mechanism revealed here suggests that highly anisotropic exfoliation energy might be prevalent in many other 1D crystals with similar structures. Consequently, simple exfoliation could be utilized to produce 1D physical systems easily.

Our experimental findings indicate that TNS nanowires can achieve lengths of several millimeters while exhibiting consistent crystalline structure. Moreover, the density of states of TNS was investigated using DFT calculations (Figure S8), which indicated the presence of a semiconducting gap with a magnitude of 0.24 eV. The findings collectively suggest that TNS can be utilized to develop electronic devices for various prospective applications. Hence, we demonstrate the feasibility of fabricating nanoelectronics directly onto a single nanowire using standard lithographic procedures. The typical protocol starts with transferring the nanowire onto a silicon wafer, followed by lithography, and finishes with metallization and lift-off to attain the ultimate device. AFM characterizations were conducted to examine the integrity and uniformity of device segments. As shown in Fig. 5b, the vertical patterns, 1.5 μm wide and 3 μm spaced, are one hundred microelectrodes designed to connect the nanowire to external instruments. Across all the one hundred microelectrodes, the 203 nm thick nanowire exhibits a minor thickness fluctuation of 2.5 nm over the entire length of 1.5 mm. This indicates that a high degree of uniformity is maintained after the series of fabrication processes. Moreover, the SEM examination shows no fractures or disconnections within the metal electrodes and nanowire, as seen in Fig. 5c. In addition, all contacts between microelectrodes and the nanowires were probed to be conductive. The details of the measurement of individual devices will be discussed in the following sections. Finally, as depicted in Fig. 5a, bonding pads extended from each microelectrode can be successfully realized, and the manufacturing of nanodevices at the chip level may be achieved. Our device fabrications underscore the remarkable potential for manufacturing an extensive array of functional devices on a single nanowire.

Given the nascent research stage on TNS, understanding the TNS/metal interface (i.e., the contact) is crucial for its potential applications. Typically, the interface can be an ohmic contact that easily allows carrier transport across the interface, making it ideal for field effect transistor applications. Conversely, a Schottky barrier interface rectifies the charge transport. It has the potential to be designed and utilized as functional building blocks in various applications, including rectifiers, logic gates, solar cells, photodetectors, and biosensors[42–49] A
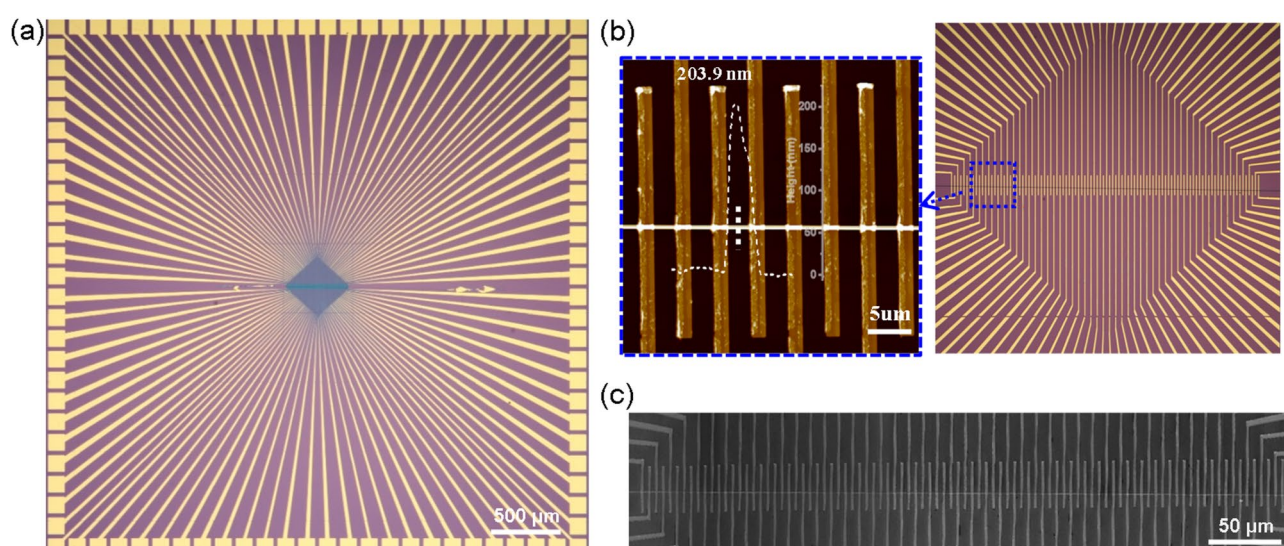

Fig. 5. One-dimensional device array on a single ultralong Ta$_2$Ni$_3$Se$_8$ nanowire. (**a**) Optical micrograph of 100 lithographically defined Au contacts distributed radially on a single nanowire. (**b**) Right: An enlarged optical view of the central segment is highlighted in (**a**). Left: representative AFM height map from the boxed region, showing a uniform nanowire thickness of ≈ 204 nm beneath consecutive electrodes and confirming the consistency of the contact fabrication. Additional AFM scans taken at other positions along the wire give comparable profiles, indicating that the uniformity is maintained along the entire device array. (**c**) SEM image of the complete device string, illustrating the regular spacing and geometry of all 100 contacts.
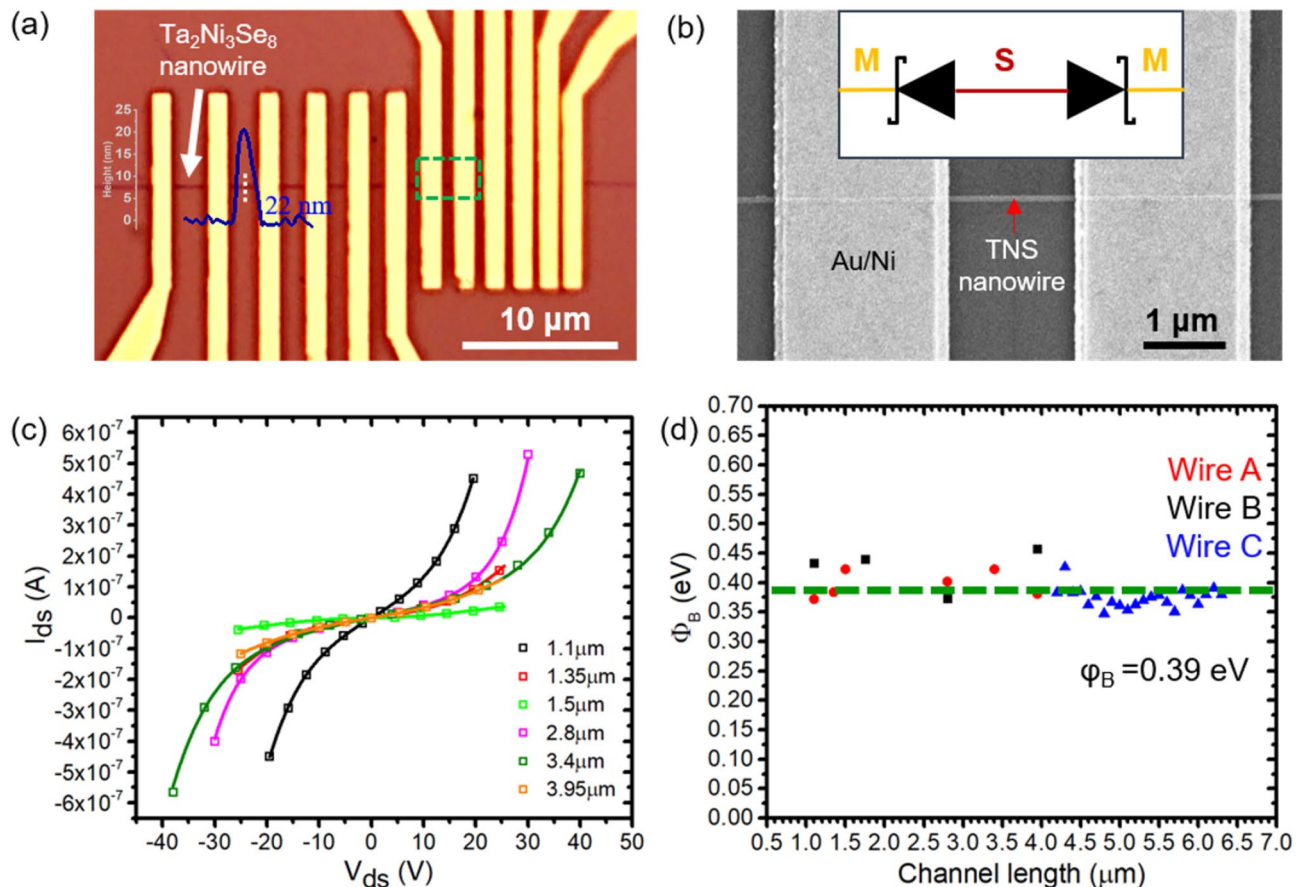
Fig. 6. Electrical characterization of Schottky devices made on TNS nanowire. (**a**) Optical image of TNS 2T devices fabricated from a single TNS nanowire. (**b**) SEM image of the M-S-M device marked in the green dashed box in (**a**) with a channel length of 1.5 μm. The inset shows the schematic of an M-S-M device structure. (**c**) Experimental I–V characteristics of TNS nanowire devices with different channel lengths (empty squares) and the fitting with the M-S-M model (solid lines). (**d**) Extracted Schottky barrier heights for devices with different TNS nanowires.

wide range of metallic materials can be employed to examine the interface's electrical properties. However, in the context of device manufacturing, forming a robust contact interface is of utmost importance. To realize this goal, we chose nickel as our primary focus. This is inspired by the study[50] of Ni clusters, wherein the emerging strong adhesion between Ni atoms is attributed to the orbital overlap of their active 3d electrons. Consequently, it is anticipated that a robust connection will be established between the Ni metal and the Ni edge of TNS nanowires.

To directly study the TNS/Ni interface, we adopted a simple two-terminal (2T) device structure composed of only three serially connected components, a central TNS nanowire, and two ends of the TNS/Ni interface for electrical characterization. Following the fabrication procedure mentioned above, a representative multi-segment 2T device on a single nanowire can be realized, as shown in the optical micrograph of Fig. 6a. The individual nanowire was contacted with 2 μm wide metal contacts with variable spacing ranging from 1 to 4 μm. The fabrication quality is further checked with SEM imaging, as shown in Fig. 6b. The single crystal nanowire and Ni contacts remained uniform and clean after fabrication, consistent with the result mentioned above from the chip-level device fabrication.

To characterize the contact properties, we performed conventional I–V measurements on each 2T device by sweeping the voltage while recording the corresponding current between two adjacent metal contacts. The typical I–V characteristics from 2T devices with different channel lengths residing on a single TNS nanowire were obtained, as shown in Fig. 6c. It is evident that all the I–V curves exhibit a superlinear characteristic, in which the current increases slowly until the voltage passes a certain threshold. This behavior indicates a barrier formation, which could result from various factors, including an insulating layer between TNS and Ni, the interfacial disorder and surface states, the Schottky barrier, and the semiconductor nanowire itself[51,52] Nevertheless, the complication at the TNS/Ni device can be simplified using an effective device model, in which the Metal-Semiconductor-Metal (M-S-M) device structure is represented by two back-to-back aligned effective Schottky diodes connected in series to one semiconductor, as illustrated in the inset of Fig. 6b. Here, the effective Schottky diode is needed because the metal-to-semiconductor (M-S) barrier height generally deviates from an ideal Schottky barrier due to the interfacial insulating layer, the image force, the thermal activation, and other possible factors. Therefore, it is further defined as a parallel shunt resistance parallelly connected

with an effective Schottky barrier, in which an ideality factor is used to count for the deviation from an ideal Schottky barrier. Furthermore, it is worth noting that the device's I–V characteristics may reflect not only the interface barrier properties but also the intrinsic properties of the nanowire itself, such as resistivity, doping concentration, mobility, defects, and electron-electron interactions. Additionally, quantum confinement effects should be ruled out since the typical thickness of nanowires is above 22 nm, much larger than the de Broglie wavelength. Other quantum effects, such as Luttinger liquid and single electron tunneling, should also be excluded because the characterization is performed at room temperature. By taking into account these factors, the utilization of thermionic field emission (TFE) theory in analyzing a Metal-Semiconductor-Metal (M-S-M) device structure effectively captures its essential attributes and provides a comprehensive explanation for a range of I–V characteristics. These characteristics encompass near-linear, near-symmetric, asymmetric, and rectifying behaviors, as demonstrated in previous studies involving M-S-M devices[51–57] Hence, employing the M-S-M model (See Methods for more details) to investigate the TNS/Ni interface will be suitable.

Due to the situation in which two Schottky diodes are connected in a back-to-back order, the I–V characteristic mainly reflects the reverse-biased Schottky barrier. The I–V relationship can be largely understood from the well-established Schottky barrier theory[58] While the large shunt resistance limits the transport current at a small bias, the current increases significantly at a moderate reverse bias due to the tunneling of the Schottky barrier. When the bias becomes large enough to overcome the barrier height, the charge carriers increase rapidly but are limited by the nanowire's resistance. We have conducted the M-S-M model fitting to all the I–Vs of our devices (about 32 devices with various lengths and thicknesses). Nearly all experimental I–V data can find a converging fitting. The details of data fitting of the devices from each nanowire are shown in Figures S9, S10, and S11. Figure 6c (empty squares in the plot) exhibits an example where the fitting result (solid line) agrees well with the experiment, confirming that the TFE-based M-S-M model accurately described the TNS/Ni device. Moreover, the Schottky barrier height of each device can be extracted from the fitting, as shown in Fig. 6d. Overall, the extracted Schottky barrier heights of thirty-two devices made on three nanowires exhibit an average value of 0.39 eV with a small fluctuation of ± 7%. Notably, the obtained effective Schottky barrier height values remain consistent for the devices with different channel lengths and nanowires, suggesting that Ni and TNS nanowires form a stable and uniform physical interface. This result also indicates that the synthesized TNS nanowire exhibits solid electrical properties due to the high crystallinity, structure integrity, and uniformity, as revealed by the TEM study. The uniformity of the Schottky barrier height may also be attributed to the homogeneity of the barrier interface between the single crystal nanowire and the nickel metal[59] While the intricate mechanism remains a subject for future investigation, the present findings provide insight into the potential utility of incorporating TNS Schottky devices in potential applications, such as photodetectors, solar cells, and chemical sensors.

Conclusion

In this study, we have achieved high yield growth of millimeter-long TNS nanowires via a straightforward solid-state reaction. The TNS nanowires were confirmed to be single crystals with uniform crystallinity throughout their entire length. Additionally, we demonstrated that scalable alignment of as-grown nanowires can be implemented, and mechanical exfoliation of individual as-grown nanowires can further produce nanowires with a few nanometers of thickness. DFT investigation reveals that the significant exfoliating capability of TNS nanowires originates from the considerable anisotropy in cleavage energy. Moreover, the electrical transport study of TNS nanodevices reveals that the electrical contact between Ni and TNS is of Schottky type, with a consistent barrier height of 0.39 eV. These findings open new avenues for the exploration of one-dimensional van der Waals materials and their potential utilization in advanced technologies.

Experimental section

Synthesis of TNS nanowires

TNS nanowires were synthesized using the solid-state reaction, as illustrated in Fig. 1a. Stoichiometric elemental powders of tantalum (157 mg, Alfa Aesar, 99.97% purity), nickel (76.4 mg, Alfa Aesar, 99.99% purity), and selenium (274 mg, Alfa Aesar, 99.99% purity) were mixed and placed in a quartz ampule (14×1.6 cm). The ampule was evacuated and sealed at a pressure of around 5×10^{-5} torr. Then, the ampule was placed in a tube furnace (Lindberg Mini Blue) with the powder source end positioned in the middle of the furnace. The furnace was then heated to 400 °C at a rate of 20 °C hr^{-1} and kept at this temperature for 10 h. Then, the furnace was ramped to 725 °C with a rate of 10 °C hr^{-1} and maintained at 725 °C for one week. Finally, the furnace was cooled to room temperature at ~ 12 °C hr^{-1}. Figure 1b shows the ampule after growth, in which a wool-like dark product can be seen.

Material characterization

The crystallinity of the sample was examined using a Rigaku DMAX 2200 powder diffractometer, configured with Cu Kα radiation operating at 40 kV and 40 mA with a scan rate of 1º min$^{[-1]}$. The chemical composition was confirmed with EDS (Oxford Instruments) attached to SEM (Hitachi S-3400) operating at an accelerating voltage of 30 kV. The morphology and nanostructure of the samples were characterized by SEM (Hitachi S4800) working at an acceleration voltage of 10 kV and TEM (Tecnai G2-F30). All TEM images and SAED patterns were taken at an accelerating voltage of 300 kV. The thickness of nanowires was determined using AFM (Bruker Dimension ICON).

First-principles calculations

DFT calculations are performed within the projector augmented wave method[60] as implemented in the Vienna Ab-initio Simulation Package[61,62] The generalized gradient approximation (GGA) functional with the Perdew-

Burke-Ernzerhof parametrization[63] is used. A plane-wave energy cut-off is set to 400 eV. Structural relaxation is done until the forces acting on each atom become less than 10^{-3} eV/Å. An accurate computational description of the $M_2X_3Y_8$ nanoribbons system is conjugated with a proper choice of vdW dispersion functional. Here, we test 4 possible cases, including (i) vdW is switched off, (ii) DFT-D3 semi-empirical method,[64] (iii) non-local VDW-DF1 method,[65] and (iv) fractional ionic atoms (FIA) method[66] The latter is currently proposed to be one of the best nowadays,[67] especially in the presence of pronounced atomic polarizability that should take place in nanoribbon systems. Inter-chain E_{bind} is intrinsically found as the normalized energy difference between the bulk system and two single ribbons that form a bulk unit cell.

$$E_{bind} = -\frac{E_{bulk} - 2\times E_{single}}{4} \tag{1}$$

Results from different approacheS in Table S1[19,20,34] and we can see that the absence of vdW functional significantly underestimates binding energy. At the same time, all three compared vdW methods provide a consistent range of E_{bind} (1 – 1.4 eV/bond) and bond length (2.4–2.7 Å). Also, our data reveals relatively close E_{bind} and d_{inter} values for FIA and DFT-D3 methods. Since vdW corrections do not explicitly influence electronic properties, we used a less time-consuming DFT-D3 approach.

Finally, DFT-D3[64] functional is applied to describe weak interactions in the nanoribbons system adequately. The intra-bond E_2–E_4 (as well as E_1 for comparison) is evaluated through surface cleavage with necessary bonds following the equation:

$$E_{cleavage} = \frac{E_{slab} - E_{bulk}}{N_{bonds}} \tag{2}$$

where E_{slab} is the total energy of the cleaved TNS slab, E_{bulk} is bulk TNS energy, and N_{bonds} is the number of broken bonds relevant to exfoliation. To be noted, in Figure S7(f) cleavage path includes both E_4 and E_1 bonds. Therefore, subtraction of extra-E_1 bonds is applied to find E_4 cleavage energy solely.

The Brillouin zone is sampled according to the Monkhorst–Pack scheme[68] with a k-point spacing of 0.15 Å^{-1} and 0.07 Å^{-1} in the periodic directions for structural relaxation and DOS calculations, respectively. To avoid spurious interactions between the neighboring unit cells, we set the vacuum size along the non-periodic direction more than 20 Å while calculating single ribbons and TNS slabs. Found results are checked to be not influenced by spin-polarized calculations. More details on the theoretical approaches used are presented in the Supporting Information.

Device fabrication and electrical characterization

To fabricate the TNS nanodevice, we first created a multi-terminal contact pattern over an exfoliated thin nanowire by standard electron beam lithography (Raith Voyager 100). Then, a metal deposition of 75 nm nickel and 25 nm gold as the contact metal was conducted with an electron beam evaporator (Angstrom Engineering Nexdep) with a deposition rate of 0.5 Å s^{-1}. Before metal deposition, samples were ion-milled (AJA ion miller) using argon gas for 7s to remove residual PMMA layers and surface contaminants. We loaded samples immediately (within 1–2 min) into an e-beam evaporation system for metal deposition, followed by a lift-off process. Transport measurements were conducted in the ambient environment using a semiconductor parameter analyzer (HP 4155 A). Current-voltage characteristics were fitted using MATLAB-based software PKUMSM. m[69,70], to determine the Schottky barrier heights. The PKUMSM software inputs are the TNS nanowire's physical dimensions and E_0 (obtained by fitting the linear region in $\ln(I_{ds})$ vs. V).

Data availability

All data generated or analyzed during this study are included in this published article. Additional raw data files are available from the corresponding author upon reasonable request.

References

1. Mak, K. F., Lee, C., Hone, J., Shan, J. & Heinz, T. F. Atomically thin MoS_2: A new Direct-Gap semiconductor. *Phys. Rev. Lett.* **105** (13), 136805. https://doi.org/10.1103/PhysRevLett.105.136805 (2010).
2. Qian, X., Liu, J., Fu, L. & Li, J. Quantum spin hall effect in two-dimensional transition metal dichalcogenides. *Science* **346** (6215), 1344–1347. https://doi.org/10.1126/science.1256815 (2014).
3. Ross, J. S. et al. Electrical control of neutral and charged excitons in a monolayer semiconductor. *Nat. Commun.* **4** (1), 1474. https://doi.org/10.1038/ncomms2498 (2013).
4. Chen, Y. J., Cain, J. D., Stanev, T. K., Dravid, V. P. & Stern, N. P. Valley-polarized exciton–polaritons in a monolayer semiconductor. *Nat. Photonics.* **11** (7), 431–435. https://doi.org/10.1038/nphoton.2017.86 (2017).
5. Mak, K. F., Xiao, D. & Shan, J. Light–valley interactions in 2D semiconductors. *Nat. Photonics.* **12** (8), 451–460. https://doi.org/10.1038/s41566-018-0204-6 (2018).
6. Dai, J. & Zeng, X. C. Titanium trisulfide monolayer: theoretical prediction of a new Direct-Gap semiconductor with high and anisotropic carrier mobility. *Angew. Chem. Int. Ed.* **54** (26), 7572–7576. https://doi.org/10.1002/anie.201502107 (2015). (acccessed 2022/11/28).
7. Island, J. O. et al. Titanium trisulfide (TiS_3): a 2D semiconductor with quasi-1D optical and electronic properties. *Sci. Rep.* **6** (1), 22214. https://doi.org/10.1038/srep22214 (2016).
8. Stolyarov, M. A. et al. Breakdown current density in h-BN-capped quasi-1D $TaSe_3$ metallic nanowires: prospects of interconnect applications. *Nanoscale* **8** (34), 15774–15782. https://doi.org/10.1039/C6NR03469A (2016).

9. Geremew, A. et al. Current carrying capacity of Quasi-1D ZrTe$_3$ Van der Waals nanoribbons. *IEEE Electron Device Lett.* **39** (5), 735–738. https://doi.org/10.1109/LED.2018.2820140 (2018).

10. Zhang, Q. et al. Thermal transport in Quasi-1D Van der Waals crystal Ta$_2$Pd$_3$Se$_8$ nanowires: size and length dependence. *ACS Nano.* **12** (3), 2634–2642. https://doi.org/10.1021/acsnano.7b08718 (2018).

11. Pant, A. et al. Strong dichroic emission in the pseudo one dimensional material ZrS$_3$. *Nanoscale* **8** (36), 16259–16265. https://doi.org/10.1039/C6NR05238J (2016).

12. Empante, T. A. et al. Low resistivity and high breakdown current density of 10 Nm diameter Van der Waals TaSe$_3$ nanowires by chemical vapor deposition. *Nano Lett.* **19** (7), 4355–4361. https://doi.org/10.1021/acs.nanolett.9b00958 (2019).

13. Island, J. O. et al. TiS$_3$ transistors with tailored morphology and electrical properties. *Adv. Mater.* **27** (16), 2595–2601. https://doi.org/10.1002/adma.201405632 (2015).

14. Island, J. O. et al. Ultrahigh photoresponse of Few-Layer TiS$_3$ nanoribbon transistors. *Adv. Opt. Mater.* **2** (7), 641–645. https://doi.org/10.1002/adom.201400043 (2014).

15. Wu, W. et al. Thermal localization enhanced fast photothermoelectric response in a Quasi-One-Dimensional flexible NbS$_3$ photodetector. *ACS Appl. Mater. Interfaces.* **12** (12), 14165–14173. https://doi.org/10.1021/acsami.0c00764 (2020).

16. Randle, M. et al. Gate-Controlled Metal–Insulator transition in TiS$_3$ nanowire Field-Effect transistors. *ACS Nano.* **13** (1), 803–811. https://doi.org/10.1021/acsnano.8b08260 (2019).

17. Li, W., Yang, L., Wang, J., Xiang, B. & Yu, Y. Three-Dimensionally interconnected TaS$_3$ nanowire network as anode for High-Performance flexible Li-Ion battery. *ACS Appl. Mater. Interfaces.* **7** (10), 5629–5633. https://doi.org/10.1021/acsami.5b00467 (2015).

18. Wen, X. et al. Evaluating the electrical characteristics of Quasi-One-Dimensional ZrTe$_3$ nanoribbon interconnects. *ACS Appl. Electron. Mater.* **3** (9), 4228–4235. https://doi.org/10.1021/acsaelm.1c00659 (2021).

19. Jeong, B. J. et al. Ternary transition metal chalcogenide Nb$_2$Pd$_3$Se$_8$: A new candidate of 1D Van der Waals materials for Field-Effect transistors. *Adv. Funct. Mater.* **32** (4), 2108104. https://doi.org/10.1002/adfm.202108104 (2022).

20. Liu, X. et al. Direct fabrication of functional ultrathin Single-Crystal nanowires from Quasi-One-Dimensional Van der Waals crystals. *Nano Lett.* **16** (10), 6188–6195. https://doi.org/10.1021/acs.nanolett.6b02453 (2016).

21. Liu, X. et al. High yield production of ultrathin fibroid semiconducting nanowire of Ta$_2$Pd$_3$Se$_8$. *Nano Res.* **13** (6), 1627–1635. https://doi.org/10.1007/s12274-020-2784-y (2020).

22. Sukhanova, E. V. & Sorokin, P. B. Specific response of the atomic and electronic structure of Ta$_2$Pd$_3$Se$_8$ and Ta$_2$Pt$_3$Se$_8$ nanoribbons to the uniaxial strain. *J. Phys. Chem. C.* **124** (13), 7539–7543 (2020).

23. Oh, S. et al. Inorganic molecular chain Nb$_2$Se$_9$: synthesis of bulk crystal and One-Atom-Thick level exfoliation. *Physica status solidi (RRL) – Rapid research letters* **12** (12), 1800451, (2018). https://doi.org/10.1002/pssr.201800451. DOI: https://doi.org/10.1002/pssr.201800451.

24. Purschke, D. N. et al. Ultrafast photoconductivity and Terahertz vibrational dynamics in Double-Helix snip nanowires. *Adv. Mater.* **33** (34), 2100978. https://doi.org/10.1002/adma.202100978 (2021).

25. Daniel, V. et al. Air-stable monodispersed Mo$_6$S$_3$I$_6$ nanowires. *Nanotechnology* **15** (5), 635. https://doi.org/10.1088/0957-4484/15/5/039 (2004).

26. Qu, Y. et al. High-Aspect ratio, and Free-Standing magnetic nanowires by exfoliation of ferromagnetic Quasi-One-Dimensional Van der Waals lattices. *J. Am. Chem. Soc.* **143** (46), 19551–19558. https://doi.org/10.1021/jacs.1c09607 (2021).

27. Odink, D. A., Carteaux, V., Payen, C. & Ouvrard, G. Synthesis and structure of chromium antimony triselenide (CrSbSe$_3$): a pseudo-one-dimensional ferromagnet. *Chem. Mater.* **5** (2), 237–240. https://doi.org/10.1021/cm00026a015 (1993).

28. Zhai, T. et al. Single-Crystalline Sb$_2$Se$_3$ nanowires for High-Performance field emitters and photodetectors. *Adv. Mater.* **22** (40), 4530–4533. https://doi.org/10.1002/adma.201002097 (2010).

29. Sun, Z. et al. Exfoliation, and transport properties of Quasi-1D Van der Waals fibrous red phosphorus. *Chem. Mater.* **33** (15), 6240–6248. https://doi.org/10.1021/acs.chemmater.1c02136 (2021).

30. Qin, J. K. et al. Raman response and transport properties of tellurium atomic chains encapsulated in nanotubes. *Nat. Electron.* **3** (3), 141–147. https://doi.org/10.1038/s41928-020-0365-4 (2020).

31. Lu, K. L. et al. Mechanical damage of carbon nanotubes by ultrasound. *Carbon* **34** (6), 814–816. https://doi.org/10.1016/0008-6223(96)89470-X (1996).

32. Mukhopadhyay, K., Dwivedi, C. D. & Mathur, G. N. Conversion of carbon nanotubes to carbon nanofibers by sonication. *Carbon* **40** (8), 1373–1376. https://doi.org/10.1016/S0008-6223(02)00074-X (2002).

33. Ma, P. C., Siddiqui, N. A., Marom, G. & Kim, J. K. Dispersion and functionalization of carbon nanotubes for polymer-based nanocomposites: A review. *Compos. Part A: Appl. Sci. Manufac.* **41** (10), 1345–1367. https://doi.org/10.1016/j.compositesa.2010.07.003 (2010).

34. Choi, K. H. et al. Ta$_2$Ni$_3$Se$_8$: 1D Van der Waals material with ambipolar behavior. *Small* **17** (37), 2102602. https://doi.org/10.1002/smll.202102602 (2021).

35. Guo, Y. et al. Soft-lock drawing of super-aligned carbon nanotube bundles for nanometre electrical contacts. *Nat. Nanotechnol.* **17** (3), 278–284. https://doi.org/10.1038/s41565-021-01034-8 (2022).

36. Sukhanova, E. V., Visotin, M. A., Popov, Z. I. & Sorokin, P. B. Stability and gas sensing properties of Ta$_2$X$_3$M$_8$ (X = Pd, Pt; M = S, Se) nanoribbons: A first-principles investigation. *Phys. Chem. Chem. Phys.* **22** (26), 14651–14659 (2020).

37. 동용관; 도정환; 윤호섭; 이영주; 신희균; 류광경. Synthesis and Characterization of Ta$_2$Ni$_3$Se$_8$. *Bulletin of the Korean Chemical Society 16* (9), 870–873. (1995). https://doi.org/10.5012/BKCS.1995.16.9.870

38. Novoselov, K. S. et al. Electric field effect in atomically thin carbon films. *Science* **306** (5696), 666–669 (2004).

39. Liang, T., Phillpot, S. R. & Sinnott, S. B. Parametrization of a reactive many-body potential for Mo–S systems. *Phys. Rev. B.* **79** (24), 245110. https://doi.org/10.1103/PhysRevB.79.245110 (2009).

40. Mande, C. & Nigavekar, A. X-ray spectroscopic study of chemical bonding in NiSe and NiSe 2. In *Proceedings of the Indian Academy of Sciences-Section A*, ; Springer: Vol. 69, pp 316–323. (1969).

41. Luo, Y. R. *Comprehensive Handbook of Chemical Bond Energies* (CRC, 2007).

42. Kumar, M., Singh Bhati, V., Ranwa, S., Singh, J. & kumar, M. Pd/ZnO nanorods based sensor for highly selective detection of extremely low concentration hydrogen. *Sci. Rep.* **7** (1), 236. https://doi.org/10.1038/s41598-017-00362-x (2017).

43. Hu, Y. et al. Fast-Response nanowire sensors by using Schottky contacts. *Adv. Mater.* **22** (30), 3327–3332. https://doi.org/10.1002/adma.201000278 (2010). (acccessed 2022/12/01).

44. Gui, E. L. et al. DNA sensing by Field-Effect transistors based on networks of carbon nanotubes. *J. Am. Chem. Soc.* **129** (46), 14427–14432. https://doi.org/10.1021/ja075176g (2007).

45. Fontana, M. et al. Electron-hole transport and photovoltaic effect in gated MoS$_2$ Schottky junctions. *Sci. Rep.* **3** (1), 1634. https://doi.org/10.1038/srep01634 (2013).

46. Zhou, J. et al. Piezoelectric-Potential-Controlled Polarity-Reversible Schottky diodes and switches of ZnO wires. *Nano Lett.* **8** (11), 3973–3977. https://doi.org/10.1021/nl802497e (2008).

47. Wang, X. et al. Ultrafast, superhigh gain visible-blind UV detector and optical logic gates based on nonpolar a-axial GaN nanowire. *Nanoscale* **6** (20), 12009–12017. https://doi.org/10.1039/C4NR03581J (2014). (acccessed 2022/12/02/00:45:21). From DOI.org(Crossref)

48. Han, N. et al. High-Performance GaAs nanowire solar cells for flexible and transparent photovoltaics. *ACS Appl. Mater. Interfaces.* **7** (36), 20454–20459. https://doi.org/10.1021/acsami.5b06452 (2015).

49. Soci, C. et al. ZnO nanowire UV photodetectors with high internal gain. *Nano Lett.* **7** (4), 1003–1009. https://doi.org/10.1021/nl070111x (2007).
50. Parida, P., Kundu, A. & Pati, S. K. The electronic and magnetic properties of a few transition-metal clusters. *J. Cluster Sci.* **20**, 355–364 (2009).
51. Chiquito, A. J. et al. Back-to-back Schottky diodes: the generalization of the diode theory in analysis and extraction of electrical parameters of nanodevices. *J. Phys.: Condens. Matter.* **24** (22), 225303. https://doi.org/10.1088/0953-8984/24/22/225303 (2012).
52. Zhang, Z. et al. Quantitative analysis of current–voltage characteristics of semiconducting nanowires: decoupling of contact effects. *Adv. Funct. Mater.* **17** (14), 2478–2489 (2007).
53. Rideout, V. L. A review of the theory, technology and applications of metal-semiconductor rectifiers. *Thin Solid Films.* **48** (3), 261–291. https://doi.org/10.1016/0040-6090(78)90007-X (1978).
54. Sze, S. M., Coleman, D. J. & Loya, A. Current transport in metal-semiconductor-metal (MSM) structures. *Solid State Electron.* **14** (12), 1209–1218. https://doi.org/10.1016/0038-1101(71)90109-2 (1971).
55. Rhoderick, E. H. Comments on the conduction mechanism in Schottky diodes. *Journal of Physics D: Applied Physics 5* (10), 1920. (1972). https://doi.org/10.1088/0022-3727/5/10/324
56. Cheung, S. K. & Cheung, N. W. Extraction of Schottky diode parameters from forward current-voltage characteristics. *Appl. Phys. Lett.* **49** (2), 85–87. https://doi.org/10.1063/1.97359 (1986). (acccessed 2022/12/01).
57. Nouchi, R. Extraction of the Schottky parameters in metal-semiconductor-metal diodes from a single current-voltage measurement. *J. Appl. Phys.* **116** (18), 184505. https://doi.org/10.1063/1.4901467 (2014). (acccessed 2022/12/01).
58. Rhoderick, E. H. & Williams, R. H. *Metal-semiconductor Contacts* (Clarendon press Oxford, 1988).
59. Kumar, A. et al. Barrier inhomogeneities limited current and 1/f noise transport in GaN based nanoscale Schottky barrier diodes. *Sci. Rep.* **6** (1), 27553 (2016).
60. Blöchl, P. E. Projector augmented-wave method. *Phys. Rev. B.* **50** (24), 17953–17979. https://doi.org/10.1103/PhysRevB.50.17953 (1994).
61. Kresse, G. & Furthmüller, J. Efficiency of ab-initio total energy calculations for metals and semiconductors using a plane-wave basis set. *Comput. Mater. Sci.* **6** (1), 15–50. https://doi.org/10.1016/0927-0256(96)00008-0 (1996).
62. Kresse, G. & Furthmüller, J. Efficient iterative schemes for Ab initio total-energy calculations using a plane-wave basis set. *Phys. Rev. B.* **54** (16), 11169–11186. https://doi.org/10.1103/PhysRevB.54.11169 (1996).
63. Perdew, J. P., Burke, K. & Ernzerhof, M. Generalized gradient approximation made simple. *Phys. Rev. Lett.* **77** (18), 3865–3868. https://doi.org/10.1103/PhysRevLett.77.3865 (1996).
64. Grimme, S., Antony, J., Ehrlich, S. & Krieg, H. A consistent and accurate Ab initio parametrization of density functional dispersion correction (DFT-D) for the 94 elements H-Pu. *J. Chem. Phys.* **132** (15), 154104. https://doi.org/10.1063/1.3382344 (2010).
65. Dion, M., Rydberg, H., Schröder, E., Langreth, D. C. & Lundqvist, B. I. Van der Waals density functional for general geometries. *Phys. Rev. Lett.* **92** (24), 246401. https://doi.org/10.1103/PhysRevLett.92.246401 (2004).
66. Gould, T., Lebègue, S., Ángyán, J. G. & Bučko, T. A. Fractionally ionic approach to polarizability and Van der Waals Many-Body dispersion calculations. *J. Chem. Theory Comput.* **12** (12), 5920–5930. https://doi.org/10.1021/acs.jctc.6b00925 (2016).
67. Tawfik, S. A., Gould, T., Stampfl, C. & Ford, M. J. Evaluation of Van der Waals density functionals for layered materials. *Phys. Rev. Mater.* **2** (3), 034005. https://doi.org/10.1103/PhysRevMaterials.2.034005 (2018).
68. Monkhorst, H. J. & Pack, J. D. Special points for Brillouin-zone integrations. *Phys. Rev. B.* **13** (12), 5188–5192. https://doi.org/10.1103/PhysRevB.13.5188 (1976).
69. Liu, Y., Zhang, Z. Y., Hu, Y. F., Jin, C. H. & Peng, L. M. Quantitative fitting of nonlinear Current–Voltage curves and parameter retrieval of semiconducting nanowire,nanotube and nanoribbon devices. *J. Nanosci. Nanotechnol.* **8** (1), 252–258. https://doi.org/10.1166/jnn.2008.N04 (2008).
70. Zhang, Z. Y., Jin, C. H., Liang, X. L., Chen, Q. & Peng, L. M. Current-voltage characteristics and parameter retrieval of semiconducting nanowires. *Appl. Phys. Lett.* **88** (7), 073102. https://doi.org/10.1063/1.2177362 (2006).

Acknowledgements

Author contributions

A.J. carried out the main part of the experimental work, including the crystal growth and characterization, device fabrication and measurement, and manuscript writing. F.W. performed the device fabrication and electrical characterization, and S. Y. and K. B. optimized the crystal growth and characterization. Y. L. performed the exfoliation experiment. K. L. and L. A. conducted the first-principal calculation and wrote part of the manuscript. J. W. designed and supervised the whole experiment. P. S. supervised the calculation part of the research. All the authors were involved in reviewing and editing the manuscript.

Declarations

Competing interest

The authors declare no competing interests.

Additional information

Supplementary Information The online version contains supplementary material available at https://doi.org/10.1038/s41598-025-03238-7.

Correspondence and requests for materials should be addressed to J.W.

Reprints and permissions information is available at www.nature.com/reprints.

Publisher's note Springer Nature remains neutral with regard to jurisdictional claims in published maps and institutional affiliations.